

Optical Engineering

OpticalEngineering.SPIEDigitalLibrary.org

Low open fraction coded masks for x-ray backscatter imaging

Andre Arelius Marcus Muñoz

Anna Vella

Matthew J. F. Healy

David W. Lane

Ian Jupp

David Lockley

SPIE.

Andre Arelius Marcus Muñoz, Anna Vella, Matthew J. F. Healy, David W. Lane, Ian Jupp, David Lockley,
“Low open fraction coded masks for x-ray backscatter imaging,” *Opt. Eng.* **57**(9), 093108 (2018),
doi: 10.1117/1.OE.57.9.093108.

Published by SPIE. This is the Author Accepted Manuscript issued with: Creative Commons Attribution Non-Commercial License (CC:BY:NC 4.0).
The final published version (version of record) is available online at DOI:10.1117/1.OE.57.9.093108. Please refer to any applicable publisher terms of use.

Low open fraction coded masks for x-ray backscatter imaging

Andre Arelius Marcus Muñoz,^{a,*} Anna Vella,^a Matthew J. F. Healy,^a David W. Lane,^a Ian Jupp,^b and David Lockley^b

^aDefence Academy of the United Kingdom, Cranfield University, Cranfield Forensic Institute, Shrivenham, United Kingdom

^bDefence Science and Technology Laboratory, Counter Terrorism and Security Division, Fort Halstead, United Kingdom

Abstract. Previous research has indicated that coded masks with open fractions <0.5 are optimal for imaging some types of far-field scenes. The open fraction, in this case, refers to the ratio of open elements in the mask, with values <0.5 considered as low open fraction. Research is limited by the sparsity of <0.5 open fractions masks; thus a further 94 lower open fraction arrays are calculated and presented. These include the dilute uniformly redundant array and singer set, along with information on imaging potential, array sizes, and open fractions. Signal-to-noise ratio reveals the 0.5 open fraction modified uniformly redundant array to be the optimal coded mask for near-field x-ray backscatter imaging, over the lower open fraction singer set, dilute uniformly redundant and random array. © 2018 Society of Photo-Optical Instrumentation Engineers (SPIE) [DOI: 10.1117/1.OE.57.9.093108]

Keywords: coded apertures; coded masks; x-ray backscatter; low open fraction.

Paper 180678 received May 9, 2018; accepted for publication Aug. 30, 2018; published online Sep. 24, 2018.

1 Introduction

Coded mask (CM) or coded aperture (CA) imaging can be traced back as far as the 1960s when they were primarily used for high-energy astronomy.^{1,2} Other applications of coded mask imaging (CMI) are found in medical imaging,³ defense, and security.⁴ CMs are based on two-dimensional (2-D) binary arrays of 1 and 0 elements. Each 1 element of the array represents an open region or aperture in the physical mask, whereas 0s are regions opaque to radiation. The ratio of open elements in the array to the total number of elements is known as the “open fraction,” “aperture transmission,” or “aperture density.”⁵ Patterns such as the modified uniformly redundant array (MURA)⁶ have an open fraction (ρ_ϕ) of 0.5 and are arguably the most common type used in CMI. This is because the MURA’s theoretical point spread function (PSF) is ideal for imaging, containing flat side-lobes and plateau/background.

Previous publications have proposed a possible relationship between open fractions and capacity to image different scenes. The uniformly redundant array (URA)⁷ contains “higher” open fractions of $\rho_\phi \geq 0.5$, which allow a greater throughput of radiation and are ideal for low-intensity sources.⁷ An aperture density $\rho_\phi < 0.5$ is termed “lower open fraction” (LOF) and has been postulated to produce optimum results with low background scenes for a point source.⁸ Studies using simulated results from the “Satellite per Astronomia a raggi X” (satellite for x-ray astronomy) wide field camera (SAX-WFC) reveal optimum signal-to-noise ratio (SNR) for LOFs between $\rho_\phi = 0.25$ and 0.33 for faint sources.⁹ It must be noted that the above research was based on point source or far-field imaging. Concerning imaging in the near-field (at closer ranges) with complex scenes, research using a $\rho_\phi = 0.5$ MURA presented superior results over LOF arrays such as the no-two-holes-touching (NTHT) version of a MURA¹⁰ and “new system” array.^{11,12} Similar findings were also found when comparing the

$\rho_\phi = 0.5$ MURA with the other LOF arrays used for x-ray backscatter imaging.¹³

The $\rho_\phi = 0.5$ URA exhibits perfect PSF properties and has advantages over most, if not all LOF arrays published to date. Indeed, finding LOF masks with similar PSF as the URA is challenging, and none of them are known to exist thus far.^{5,9,12,14} Also, the number of published LOF arrays with good PSF is limited in vector size (except the random array). A publication of “LOF URAs” from Busboom et al.⁵ and the singer set array (Shutler et al.¹⁵) demonstrates the limited number of such arrays, with a total of ~ 99 different array sizes of varying open fractions. Based on these findings, this paper seeks to address limitations by presenting design rules for additional 94 LOF arrays in the form of the singer set and dilute uniformly redundant array¹⁶ (DURA). Also, x-ray backscatter exposures from a $\rho_\phi = 0.5$ MURA, $\rho_\phi = 0.43$ DURA, $\rho_\phi = 0.33$ singer set, and $\rho_\phi = 0.33$ random array (RANDA) are presented, with the SNR calculated, analyzed, and compared. The implications of this research are important because CMs can significantly decrease the exposure time of a backscatter imaging system and increase image potential. Therefore, by understanding the properties of various CMs, this may help x-ray backscatter imaging to evolve for various applications.

2 Method

2.1 Modified Uniformly Redundant Array

As the URA’s name suggests, each open region in the array is spaced equally, which makes the URA “uniformly redundant.”¹⁷ The MURA is part of the URA family and inherits the benefits of ideal imaging properties. An advantage of the MURA is that its vectors (p and q) do not obey the twin prime rule of $p \pm q = 2$ that is subjected to the URA. Consequently, the MURA’s vectors can be comprised of any prime number and follow the equation $p \pm q = 0$.¹³ All MURAs have an open fraction of ~ 0.5 ⁶ that can be

*Address all correspondence to: Andre Arelius Marcus Muñoz, E-mail: a.munoz@cranfield.ac.uk

symmetrical or nonsymmetrical. 2-D MURA patterns begin with a vector length (L), which is based on prime numbers [see Eq. (1)]:

$$L = \begin{cases} 4m + 1 & \text{for symmetric} \\ 4m + 3 & \text{for nonsymmetric} \end{cases} \quad \text{where,} \quad (1)$$

$$m = 1, 2, 3, \dots$$

A new sequence was generated [see Eq. (2)] from the vector length and then used to form a one-dimensional (1-D) binary sequence.

$$A = [A_i]_0^{L-1}. \quad (2)$$

The binary sequence must follow the condition in Eq. (3), rendering all 1s in the sequence a quadratic residue modulo L .⁶

$$A_i = \begin{cases} 0 & \text{if } i = 0 \\ 1 & \text{if } i \text{ is a quadratic residue modulo } L. \\ 0 & \text{otherwise} \end{cases} \quad (3)$$

Once the 1-D binary sequence was generated, an inverse was created for the mapping process. Subsequently, all 1s in the sequence become 0s, and all 0s become 1s [see Eqs. (4) and (5), for example, with a five vector MURA 1-D sequence]:

$$A_i = 1 \quad 1 \quad 0 \quad 0 \quad 1, \quad (4)$$

$$A'_i = 0 \quad 0 \quad 1 \quad 1 \quad 0. \quad (5)$$

The final coded array pattern is constructed by mapping the 1-D sequence A_i onto a 2-D array (M), where i and j are the components of the array's x and y vectors, respectively. Namely, the 1-D sequence was mapped in accordance with $A_{i,1} = A_{1,j}$ as shown in Fig. 1(a). Both A_i or A'_i were then mapped on rows of the 2-D array, where the first element matched those of the corresponding first column vector [see Figs. 1(b) and 1(c)]. To complete the 2-D array, $A_{i,1} = 1$, and then $A_{1,j} = 0$ [see Fig. 1(d)], and a circular-shift by $L/2$, which was rounded down to the nearest natural

number resulting in a centered MURA [see Figs. 1(e) and 1(f)]. In this case $L = 5$ and hence, indicating a circular shift of 2.5 that is rounded down to 2. The array in Fig. 1(d) is shifted down twice and to the right twice. An example is seen with element $A_{1,1}$, which is represented as a bold "0" in Fig. 1(d) is shifted to a central position $A_{3,3}$ in Fig. 1(e).

2.2 Random Array

When the elements of an array are randomly generated, it is then termed a random array (RANDA).² The PSF of RANDAs presents a raised plateau due to noise inherent to the array. Despite this, the prospect of imaging with the RANDA is rather good. Random arrays have an advantage over all other CMs in that they are versatile because nearly any open fraction, and array size can be generated. The random array used in this paper was generated in MATLAB^{®18} by creating an array of zeros. An inbuilt MATLAB[®] function then determined which elements of the array would be changed to ones, based on a given open fraction.

2.3 Dilute Uniformly Redundant Array

A dilute URA (DURA) also exhibits "uniformly redundant" properties. This is evident in the constant spacing between open regions. The 1-D sequence of a DURA is based on known Barker codes^{16,19} and limited in number. The sequence can be used to generate higher open fraction (>0.5) and LOF 2-D arrays, with the PSF sharing similar characteristics with a URA (having a flat plateau or "background") and nonredundant array (NRA).²⁰ The NRA's PSF contains a flat plateau and featured sidelobes that oscillate beyond some distance, according to previous literature.^{16,17,21} The term "nonredundant" refers to the spacing distance in open regions that do not repeat. This is only achieved with lower open fraction arrays. Published 1-D sequences for DURAs are limited to lengths (L) 13, 21, 31, 57 and 73, that follow the expression in Eq. (6), where K is the number of open elements with the sequence:

$$L = K(K - 1) + 1. \quad (6)$$

Little has been published on the construction process for 2-D DURAs, apart from Munoz et al.¹³ which only gave information on a 2-D 13 DURA. In this paper, 2-D DURAs were generated from 1-D sequences to produce 15 arrays with different vector sizes and open fractions (see Appendix for PSF). All arrays were constructed using a mapping process similar to that of the MURA in Figs. 1(a)–1(c). However, this would result in a DURA with open fractions >0.5 . Therefore, to produce arrays of LOF, the initial sequence was inverted similar to Eqs. (4) and (5), respectively. Consequently, Fig. 1(a) began with the inverted sequence and Figs. 1(b) and 1(c) were complemented by the original 1-D sequence. As a result, all DURAs from the 1-D sequence constructed in this manner were lower in open fraction.

2.4 Singer Set

Singer set arrays are part of the family of cyclic different sets^{15,22} and are sometimes referred to as "singer URAs,"⁵

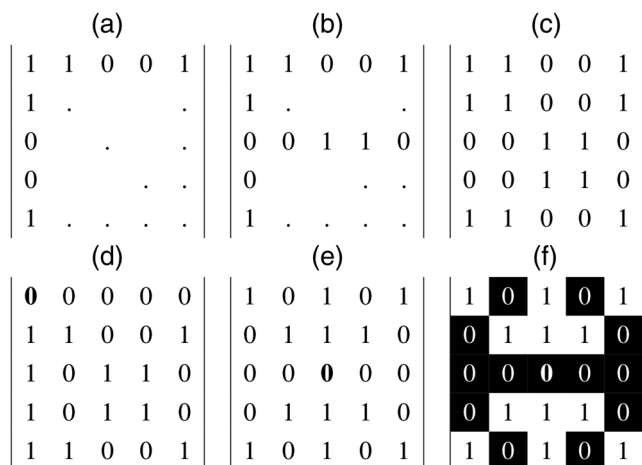


Fig. 1 (a)–(d) Mapping process of a 1-D sequence onto a 2-D array. (e) 5 MURA. (f) 5 centred MURA.

or singer, even though the arrays are not necessarily uniformly redundant. However, the term “URA” may derive from similar PSFs in some cases. The singer set poses good imaging qualities; however, they usually contain PSFs with a nonperfect and raised plateau (see Fig. 2). Shifting the vectors of a $\rho_\phi = 0.5$ 15×17 singer set array demonstrated achieving PSFs that are coherent with those from a URA. Circular shifting of individual vectors alters the original sequence (see Fig. 2). Note, this does not appear to be the case with lower open fraction singer sets thus far. Therefore, singer sets may be considered a “URA like” array as referred to in Skinner,²¹ possibly from having good imaging properties from its PSF.

Singer sets range in open fraction from $0 < \rho_\phi < 0.5$ with coprime vectors. A feedback shift register is used to generate the 1-D sequence (M_0) as in Eq. (7), where N is the number of shifts and q defining the reciprocal of the open fraction:

$$M_0 = \frac{q^N - 1}{q - 1}. \quad (7)$$

For generating the singer set in Fig. 2, a computer program “cdsngen.exe” was used to create the cyclic different sets (CDS) 1-D sequence.¹⁵ (This can be found in the Appendix section of the article.) The CDS sequence from Eq. (7) was then converted to binary following the conditions in Eq. (8) and subsequently transformed from a 1-D sequence to a 2-D array:

$$M_0 = \begin{cases} 0 & \text{if } i > 0 \\ 1 & \text{if } i = 0 \end{cases}. \quad (8)$$

Singer set array vectors are coprime.¹⁵ Therefore, M_0 must follow the conditions in Eq. (9) for the folding process to be successful, where m and n are coprime, and p is a pad value. Note, $|$ is the mathematical divisor symbol stating that there is a perfect division with no remainder and \nmid is when a perfect division is not possible:

$$m \times n = \begin{cases} M_0 & \text{if } m|M_0 \\ M_0 + p & \text{if } m \nmid M_0 \end{cases}. \quad (9)$$

Unlike the MURA and DURA, which is mapped from a relatively short 1-D sequence, singer sets are folded from long 1-D sequences into a 2-D array similar to the sequence (M) in Fig. 3.

$$M = 1, 2, 3, 4, 5, 6, 7, 8, 9, 10. \rightarrow M = \begin{vmatrix} 1 & 6 \\ 2 & 7 \\ 3 & 8 \\ 4 & 9 \\ 5 & 10 \end{vmatrix}$$

Fig. 3 The folding process of a hypothetical sequence M .

2.5 Lower Open Fraction Array Limitations

The notion of optimum LOF arrays for use with different imaging scenes date back as far as the 1970s, with Gunson and Polychronopoulos,⁸ and other publications in more recent times.^{9,12} Ultimately, the candidate array would be a URA due to its PSF properties or at the very least an array with a similar PSF. For the URA, this is arguably nonexistent and leaves candidates with “URA like” qualities, which are still rather limited in vector size and open fraction. This was demonstrated by Busboom et al.⁵ Also, a nonexhaustive list of singer sets has been published by Shutler et al.¹⁵ who presented a plot of the 14 LOF singer sets of up to 100 elements (see Appendix). It must be clear that LOF arrays are not limited to those presented by Busboom and Shutler et al., and some arrays published elsewhere were not included, such as the NRA and DURA.

2.6 Encoding and Decoding Process

A selection of coded arrays was chosen based upon their PSF and relative vector sizes. This included a 19 random array with $\rho_\phi = 0.33$, 13 DURA with $\rho_\phi = 0.43$, 17×21 singer set with $\rho_\phi = 0.33$, and a 19 MURA $\rho_\phi = 0.5$ used as a standard of measure. Physical coded masks of different sizes with their smallest elements size measuring 2 mm were fabricated from the array patterns, using three-dimensional (3-D) printed polylactic acid and a tungsten/epoxy.^{23,24} The advantages of this over the traditional machined drilled tungsten versions are that they retain their true open fraction value and the apertures have an ideal square aspect ratio. This is critical when comparing open fractions because NTHT versions naturally change the open fraction of the original mask to a lower value.

The equipment used in the experiment was a VJ Technology^{®25} x-ray source producing radiation at 100 kV and 5 mA. Also, a Photonic-Sciences[®] Gemstar²⁶ x-ray sensitive 1.4 megapixel detector was used to expose backscattered

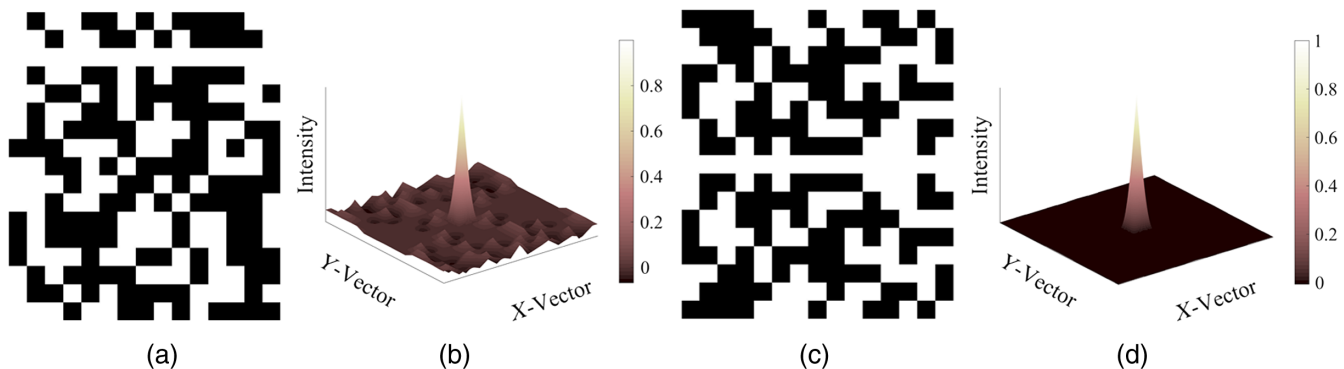


Fig. 2 (a) 15×17 singer set and (b) PSF. (c) 15×17 singer set with vectors circular shifted to achieve symmetry along the Y-axis, along with (d) PSF.

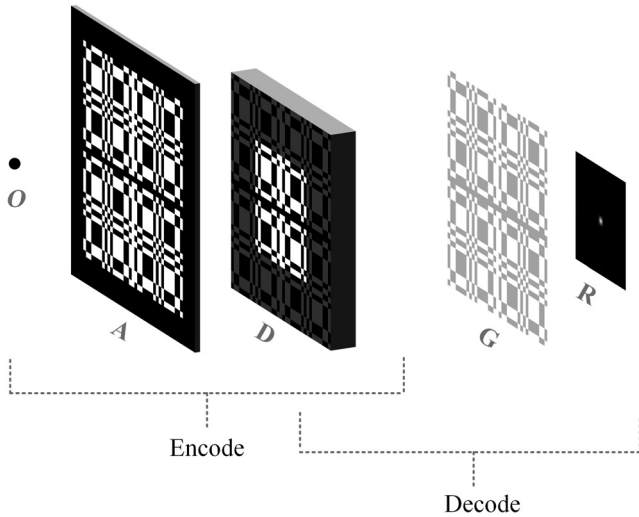


Fig. 4 Encoding and decoding process, where the object (O), encoding array (A), detector (D), decoding array (G), and reconstructed image (R) are presented.

x-rays. Two five second x-ray backscatter exposures (D) of a scene/object (O), which was four blocks placed in front of a lead screen to provide a uniform background, were captured with each CM (A), which completed the encoding process (see Fig. 4).²⁷ One exposure was taken with the CM in its normal orientation and another rotated at 90 deg. The purpose of this was to sum both exposures, intensifying the signal and reducing/canceling noise within the final image.²⁸ All masks were mosaicked by repeating the original unit or base pattern twice in the X- and Y-directions of the array so that a total of four patterns were present. The mosaic had one row and one column removed, so only one full unit pattern (full cycle) was present. Subsequently, the overall aim was to minimize the effects of partially coded field of view.^{4,29}

Encoded exposures were ultimately cropped to the size of the unit or base pattern of the encoding array. Such an act was performed to remove artifacts presented by the mosaic.³⁰ Due to imaging at close range, near-field magnification (N_m) was applied to the encoded exposure [see Eq. (10)], where (a) was the distance from O to A and (b) represented the distance from A to D (see Fig. 4):

$$N_m = \frac{a + b}{a}. \quad (10)$$

Image reconstruction (R) took place using normalized cross correlation of both the D and decoding array (G), where the bar over D and G representing the mean [see Eq. (11)]. Every step in R was automated using MATLAB®:¹⁸

$$R(u, v) = \frac{\sum_{x,y} [G(x, y) - \bar{G}_{u,v}] [D(x - u, y - v) - \bar{D}]}{\sqrt{\sum_{x,y} [G(x, y) - \bar{G}_{u,v}]^2 \sum_{x,y} [D(x - u, y - v) - \bar{D}]^2}}. \quad (11)$$

The SNR was calculated using Eq. (12) for each reconstructed image.³ The mean signal (μ_S) was chosen as a sampled region of interest from the object within the image. The background of the imaging scene was sampled

from an area of the lead screen, and the standard deviation (σ_B) was taken to calculate the SNR:

$$\text{SNR}_{\text{dB}} = 10 \log_{10} \left(\frac{\mu_S}{\sigma_B} \right). \quad (12)$$

3 Results

When addressing the limitation of LOF CMs, an additional 79 previously unreported singer set arrays of varying vector sizes and open fraction have been identified. These cover the full range of open fractions and are presented in Figs. 5, 12–15. An additional contribution of 15 CMs are presented in the form of DURAs and their open fractions (see Fig. 6 and the Appendix for the DURAs PSF). Combining the previous 79 singer set arrays and 15 DURAs yields a total of 94 additional LOF CMs.

DURAs can be divided into five different groups of 13, 21, 31, 57, and 73, which represent a vector length or width

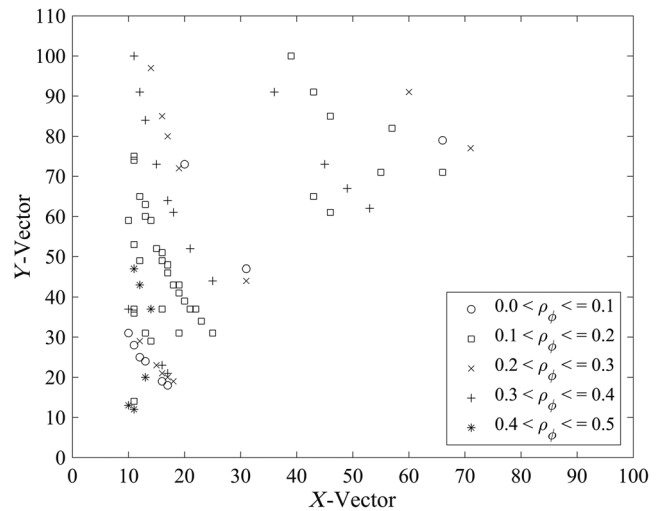


Fig. 5 Seventy-nine previously unpublished singer set arrays of open fractions <0.5 from research presented in this paper.

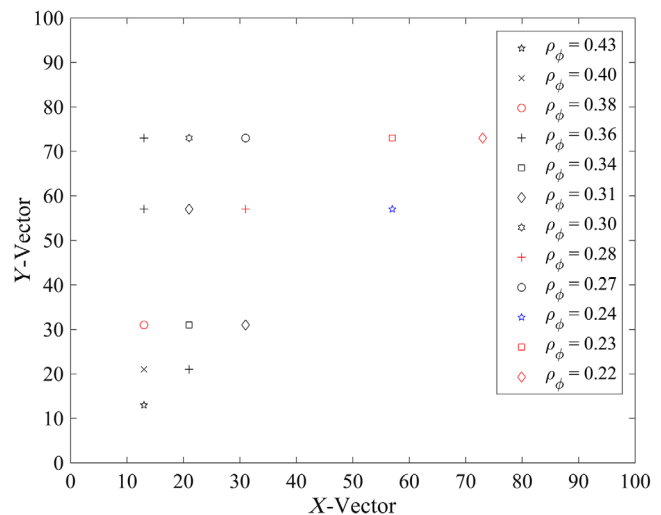


Fig. 6 Previously unpublished 2-D DURA arrays and their open fractions presented in this paper.

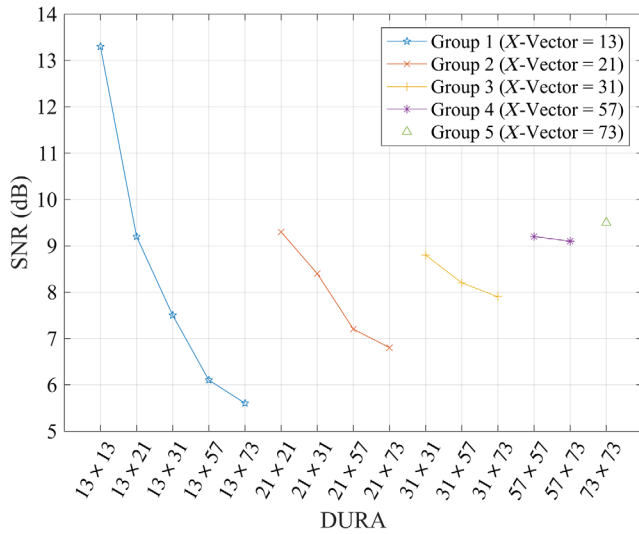


Fig. 7 Theoretical SNR of all 15 2-D DURAs.

in the 2-D array. For example, the first group of 13 contains arrays 13×13 , 13×21 , 13×31 , etc. When analyzing SNR of each array, a trend was revealed. Square arrays for each group outperformed rectangular arrays, and this was consistent with all four groups (excluding the 73 DURA, which is the only array in its group). In addition, the 13 DURA yielded the most desirable imaging properties (see Fig. 7).

Reconstructed x-ray backscatter CM exposures of a quadrant of blocks are shown in Fig. 8, which were calculated using Eq. (11). The quadrant of blocks was comprised of aluminum and wax in the upper left and right quarters,

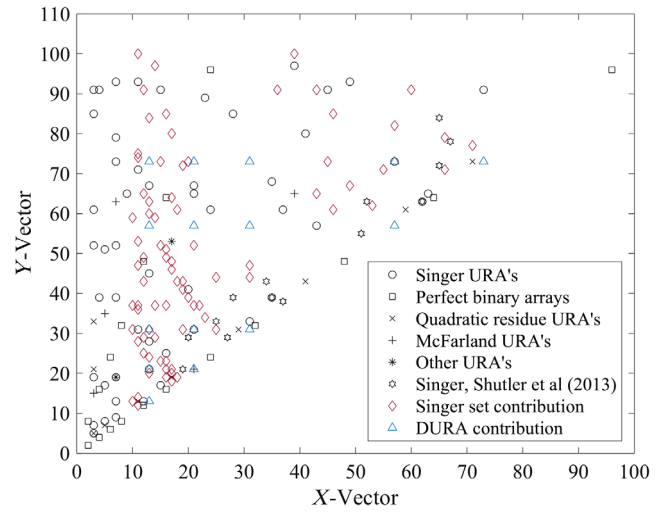


Fig. 9 Combined previously reported and contributed <0.5 low open fraction arrays.⁵

and a cylindrical PVC block and copper in the lower left and right quarter. The wax block and PVC have a bright appearance in the images due to the low atomic nature of their composition. The SNR was calculated using Eq. (12) for each reconstructed images that are as follows:

1. $\rho_\phi = 0.50$, 19 MURA with SNR = 13.6 dB.
2. $\rho_\phi = 0.33$, 17×21 singer set with SNR = 10.0 dB.
3. $\rho_\phi = 0.43$, 13 DURA with SNR = 9.6 dB.
4. $\rho_\phi = 0.33$, 19 RANDA with SNR = 9.2 dB.

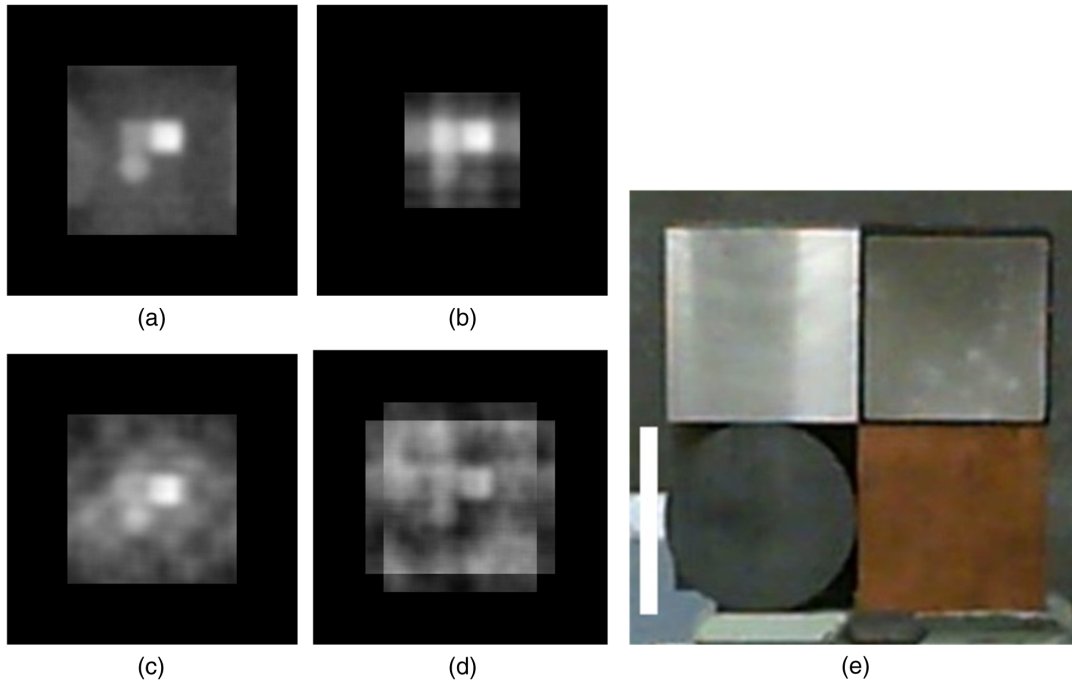


Fig. 8 X-ray backscatter expose a quadrant of blocks using 3-D printed CMs (a) 19 MURA, (b) 13 DURA, (c) 19 RANDA, and (d) 17×21 singer set. (e) An optical image of the imaging scene with a lead backdrop for the background. The CM unit pattern size determined the different sizes or field of view for each image. The white bar is a scale indicator representing 100 mm.

4 Discussion

When comparing x-ray backscatter imaging results from the $\rho_\phi = 0.5$ 19 MURA with LOF CMs in the experiment, the MURA outperformed its competitors. This trend was consistent with Accorsi et al.¹² and Munoz et al.,¹³ and can be

seen in Fig. 8. The method of obtaining SNR in Munoz et al.,¹³ involved using data from ^{241}Am radioactive source. Conversely, x-ray backscatter exposures formed the data for the experiment in this paper. Nonetheless, the trend remained consistent.

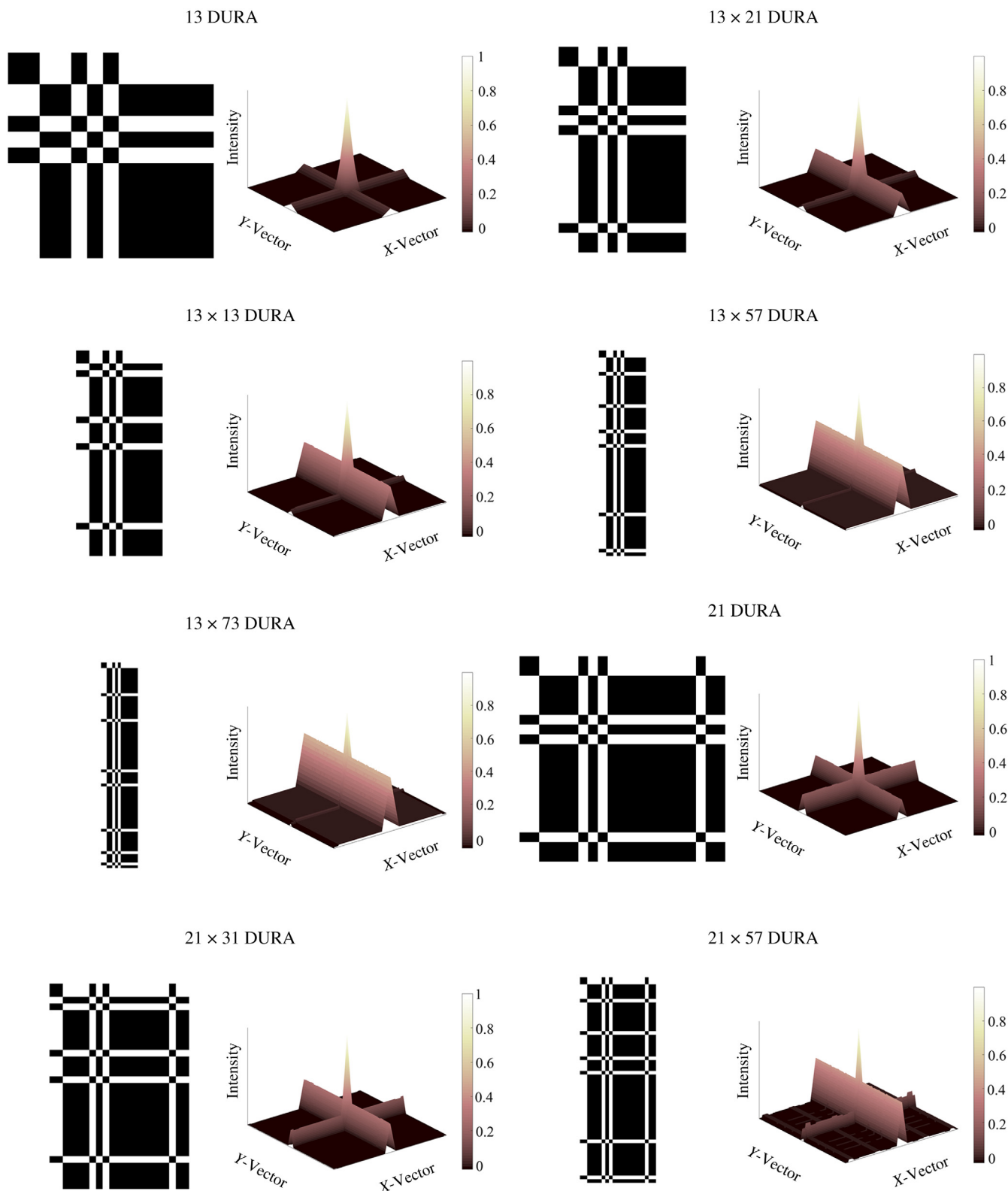


Fig. 10 13 to 21 x 57 DURA with PSF.

Similar findings were displayed in Munoz et al.,¹³ however, with the DURA performing slightly better than the singer. Results overall confirm the $\rho_\phi = 0.5$ MURA to have optimum near-field imaging properties over lower open fraction CMs. Nonetheless, it is essential to consider the possibility that the results may be specific to mask type rather than open fraction.

Limitations on the existence and abundance of URA like LOF CMs have been reported^{5,9,12,14} in previous literature.

The singer set has been at the forefront of good candidates for LOF CMs with URA qualities. However, details on the exact size and open fractions are limited, unlike the URA that is known to be $\rho_\phi = 0.5$ and based on any prime number. Previous publications have addressed such issue with information on singer set array sizes and open fraction.^{5,15} Nevertheless, variation remains limited. This paper helped solve this by declaring an additional 79 unpublished (to the best of the author's knowledge) singer sets and of various

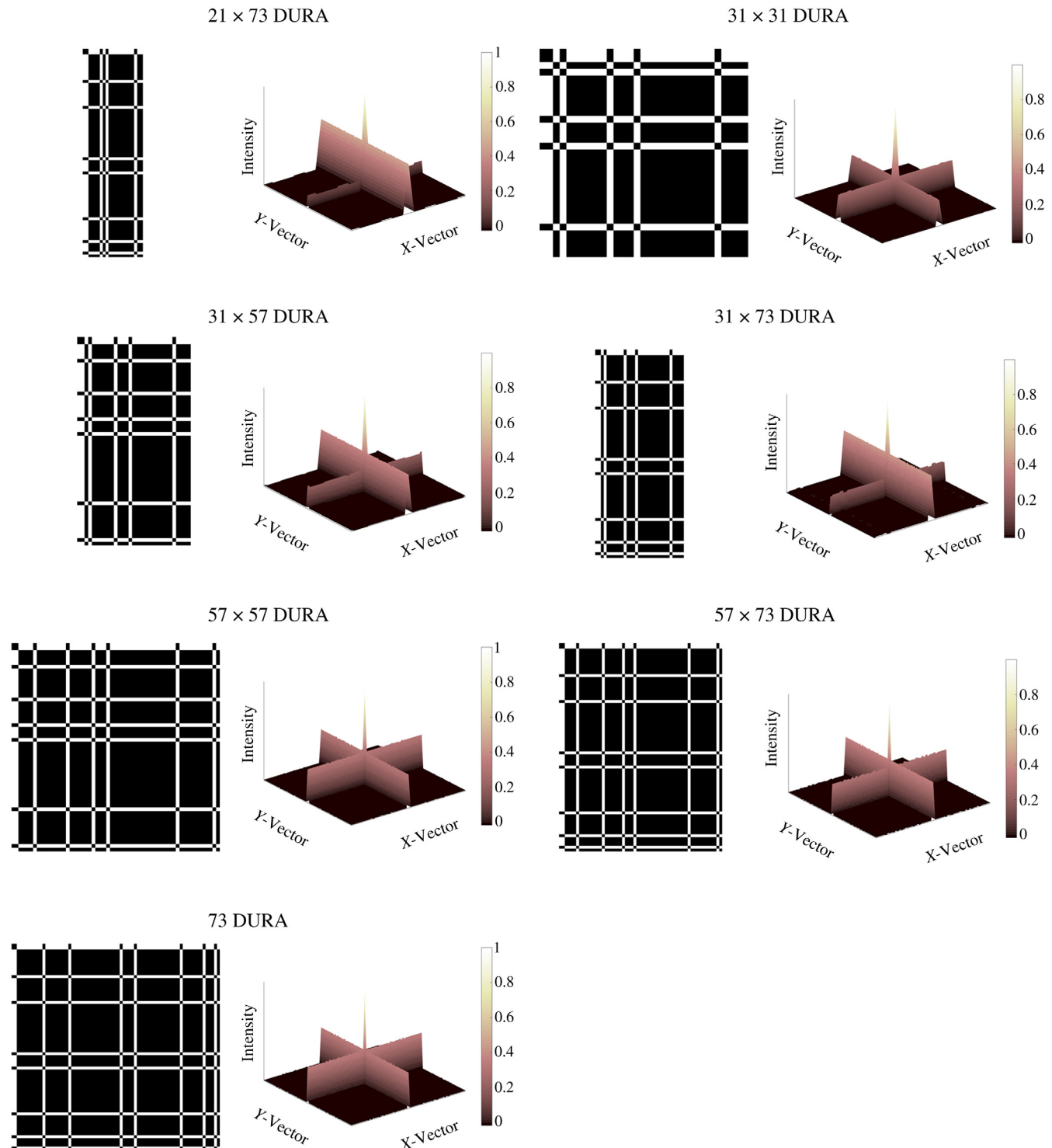


Fig. 11 21 × 73 to 73 DURA with PSF.

array sizes and LOF (see Fig. 5). Also, contributions to the list of LOF CMs have been made by presenting 15 2-D DURAs of varying array sizes and open fractions (see Fig. 6) in addition to information on their imaging properties.

5 Conclusion

The $\rho = 0.5$ MURA demonstrated superior near-field imaging capabilities over the LOF CMs. Research results appear consistent with previous work from other literature, with implications of assisting the research community to better understand the optimum mask type or open fraction for near-field x-ray backscatter imaging. The $\rho_\phi = 0.33$ 17×21 singer set ranked second to the MURA, which may demonstrate URA like imaging properties. The $\rho_\phi = 0.43$ 13 DURA followed behind the singer in SNR and could indicate the potentials of this array being a competitive candidate for imaging. Suggested future experiments would compare open fractions of the same mask type with similar array sizes. For example, using singer set masks with varying open fractions. A further contribution of 94 LOF CMs has been presented in this paper along with their

open fractions, array sizes, and construction processes. The significance of additional arrays may encourage further LOF experiments, with a more extensive choice of different arrays and open fractions. The overall impact of this research could enhance or change the way backscattered x-ray images are formed, with applications in medical imaging, industrial applications or defense, and security. The extensive range of CMs now available include many with large vector sizes that while difficult to employ in x-ray applications could find application at other wavelengths (e.g., visible light), where the demands of mask thickness are easier to accommodate.

Appendix

The known <0.5 arrays from Shutler et al. and Busboom et al.^{5,15} are presented in Fig. 9, which include the 94 previously unreported arrays introduced earlier in this study. The array patterns and PSF for the 15 2-D DURAs are shown in Figs. 10 and 11. Also, the 79 previously unpublished singer arrays presented in this paper are found in Figs. 12–15.

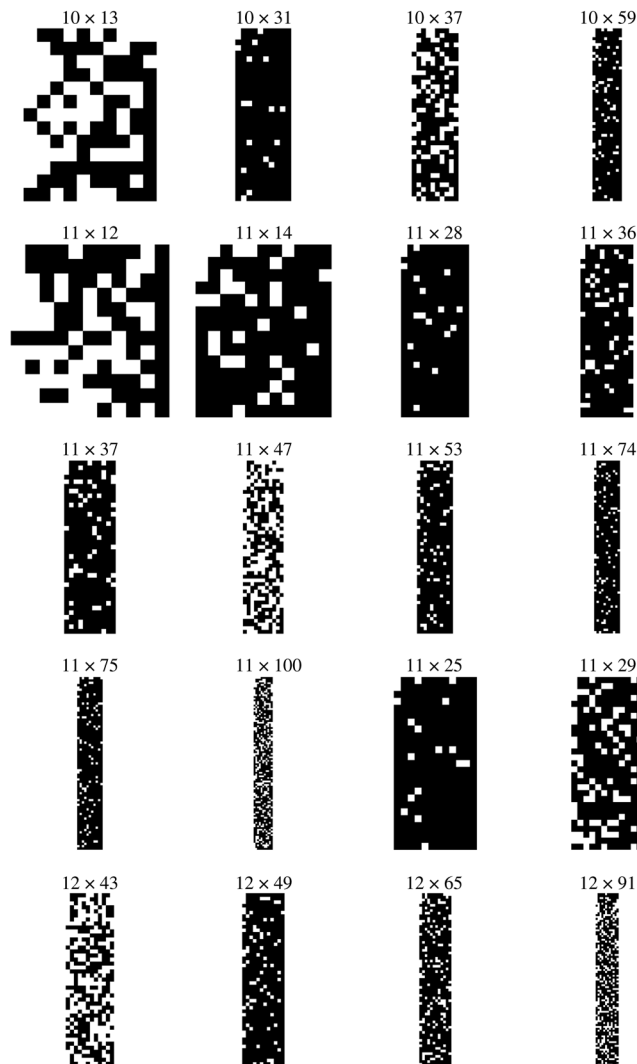


Fig. 12 Previously unpublished singer arrays presented in this paper with vectors sizes 10×13 to 12×91 .

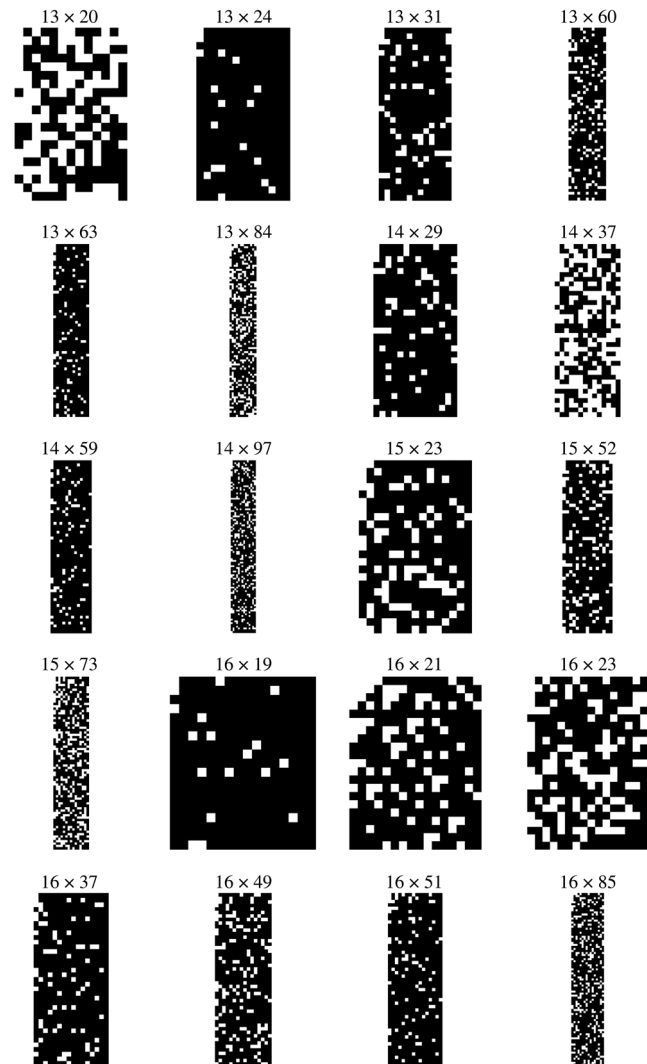


Fig. 13 Previously unpublished Singer arrays presented in this paper with vectors sizes 13×20 to 16×8 .

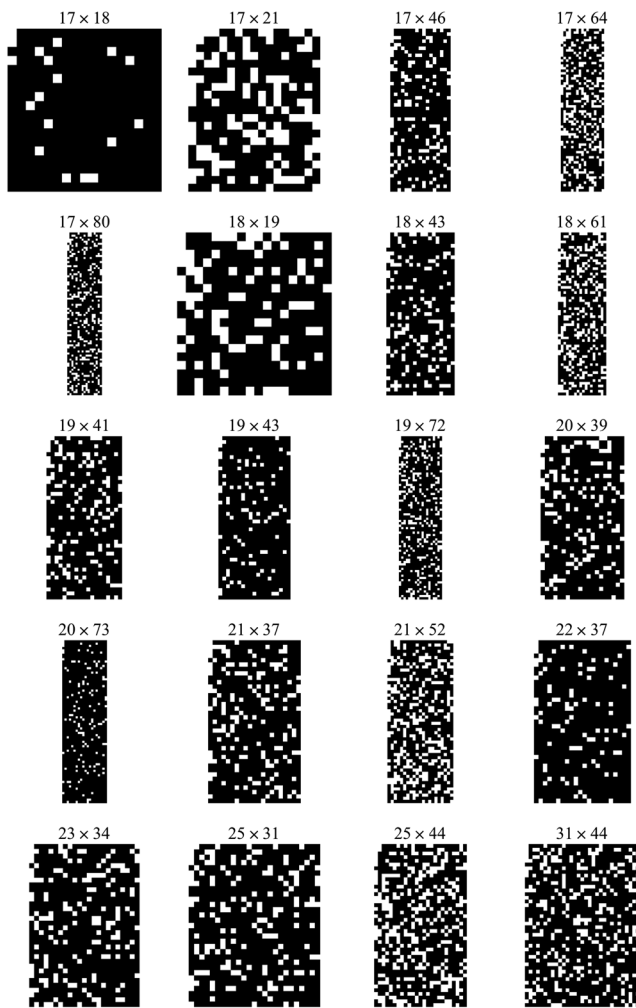


Fig. 14 Previously unpublished Singer arrays presented in this paper with vectors sizes 17×18 to 31×44 .

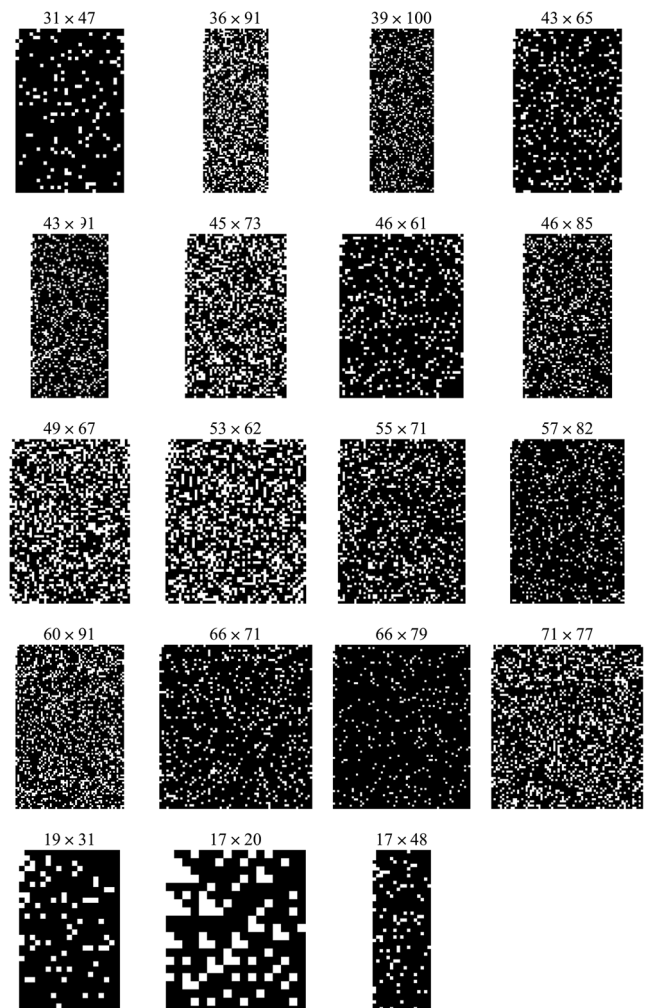


Fig. 15 Previously unpublished Singer arrays presented in this paper with vectors sizes 31×47 to 17×48 .

Acknowledgments

Content includes material subject to Crown copyright (2018), Dstl. This material is licensed under the terms of the Open Government Licence except where otherwise stated. To view this license, visit <http://www.nationalarchives.gov.uk/doc/open-government-licence/version/3> or write to the Information Policy Team, The National Archives, Kew, London TW9 4DU, or email: psi@nationalarchives.gsi.gov.uk. Defence Science and Technology Laboratory (Dstl) (DSTL/JA107335).

References

1. L. Mertz and N. O. Young, "Fresnel transformation of images," in *Optical Instruments and Techniques*, K. J. Habell, Ed., pp. 305–310, Chapman and Hall Ltd., London (1961).
2. R. H. Dicke, "Scatter-hole cameras for x-rays and gamma rays," *Astrophys. J.* **153**, L101–L106 (1968).
3. R. G. Simpson and H. H. Barrett, "Imaging for medicine," Chapter 8 in *Imaging for Medicine*, S. Nudelman and D. D. Patton, Eds., pp. 217–311, Plenum Press, New York (1980).
4. A. Faust et al., "Detection of explosive devices using x-ray backscatter radiation," *Proc. SPIE* **4768**, 17–28 (2009).
5. A. Busboom, H. Elders-Boll, and H. Schotten, "Uniformly redundant arrays," *Exp. Astron.* **8**, 97–123 (1998).
6. E. E. Fenimore and S. Gottesman, "New family of binary arrays for coded aperture imaging," *Appl. Opt.* **28**(20), 4344–4352 (1989).
7. E. E. Fenimore and T. M. Cannon, "Coded aperture imaging with uniformly redundant arrays," *Appl. Opt.* **17**(3), 337–347 (1978).

8. J. Gunson and B. Polychronopoulos, "Optimum design of a coded mask x-ray telescope for rocket applications," *Mon. Not. R. Astron. Soc.* **177**, 485–497 (1976).
9. J. In't Zand, J. Heise, and R. Jager, "The optimum open fraction of coded apertures. With an application of the wide field x-ray cameras of SAX," *Astron. Astrophys.* **288**, 665–674 (1994).
10. E. E. Fenimore and T. M. Cannon, "Uniformly redundant arrays: digital reconstruction methods," *Appl. Opt.* **20**(10), 1858–1864 (1981).
11. D. Jennings and K. Byard, "An extension for residue difference sets," *Discrete Math.* **167–168**, 405–410 (1997).
12. R. Accorsi, F. Gasparini, and R. Lanza, "Optimal coded aperture patterns for improved SNR in nuclear medicine imaging," *Nucl. Instrum. Methods Phys. Res. Sect. A* **474**, 273–284 (2001).
13. A. A. M. Munoz et al., "X-ray backscatter radiography with lower open fraction coded masks," *Proc. SPIE* **10393**, 103930A (2017).
14. A. Busboom, H. Elders-Boll, and H. D. Schotten, "Combinatorial design of near-optimum masks for coded aperture imaging," in *ICASSP, IEEE Int. Conf. on Acoustics, Speech and Signal Processing—Proc.*, Vol. 4, pp. 2817–2820 (1997).
15. P. M. E. Shutler, S. V. Springham, and A. Talebitaher, "Mask design and fabrication in coded aperture imaging," *Nucl. Instrum. Methods Phys. Res. Sect. A* **709**, 129–142 (2013).
16. W. J. Wild, "Dilute uniformly redundant sequences for use in coded-aperture imaging," *Opt. Lett.* **8**(5), 247–249 (1983).
17. R. Accorsi, "Design of near-field coded aperture cameras for high-resolution medical and industrial gamma-ray imaging," PhD Thesis, Massachusetts Institute of Technology (2001).
18. MathWorks, "MATLAB" (2018), <http://uk.mathworks.com/products/matlab/> (24 January 2016).
19. R. H. Barker, "Group synchronizing of binary digital sequences," in *Communication Theory*, S. Goswami et al., Eds., pp. 273–287, Butterworth, London (1953).

20. M. Golay, "Point arrays having compact, nonredundant autocorrelations," *J. Opt. Soc. Am.* **61**, 272–273 (1971).
21. G. K. Skinner, "Imaging with coded-aperture masks," *Nucl. Instrum. Methods Phys. Res.* **221**, 33–40 (1984).
22. P. Shutler, S. Springham, and A. Talebitaher, "Periodic wrappings in coded aperture imaging," *Nucl. Instrum. Methods Phys. Res.* **738**, 132–148 (2014).
23. A. M. A. Muñoz et al., "3D-printed coded apertures for x-ray backscatter radiography," *Proc. SPIE* **10393**, 103930F (2017).
24. A. A. M. Muñoz et al., "Rapid prototyping coded masks for x-ray backscatter imaging," *Opt. Eng.* **57**(8), 085104 (2018).
25. VJT, "VJ technology" (2017), <http://www.vjt.com/> (25 June 2017).
26. Photonic Science, "Gemstar x-ray camera" (2017), <http://www.photonic-science.co.uk/> (25 June 2017).
27. V. Paradiso et al., "A versatile calibration procedure for portable coded aperture gamma cameras and RGB-D sensors," *Nucl. Instrum. Methods Phys. Res. Sect. A* **886**, 125–133 (2018).
28. M. J. DeWeert and B. P. Farm, "Lensless coded aperture imaging with separable doubly Toeplitz masks," *Proc. SPIE* **9109**, 91090Q (2014).
29. E. Caroli et al., "Coded aperture imaging in x- and gamma ray astronomy," *Space Sci. Rev.* **45**, 349–403 (1987).
30. I. Jupp, "The optimisation of discrete pixel coded aperture telescopes," PhD Thesis, pp. 42–43, University of Southampton (1996).

Biographies for the authors are not available.

Low open fraction coded masks for x-ray backscatter imaging

Munoz, Andre Arelius Marcus

2018-09-24

Attribution-NonCommercial 4.0 International

Munoz AAM, Vella A, Healy MJF, Lane DW, Jupp I & Lockley D., Low open fraction coded masks for x-ray backscatter imaging, Optical Engineering, Volume 57, Issue 9, Article Number 093108.

<https://doi.org/10.1117/1.OE.57.9.093108>

Downloaded from CERES Research Repository, Cranfield University